Available online at www.sciencedirect.com
SCIENCE DIRECT
Journal of Magnetic Resonance 180 (2006) 163–169
JMR Journal of Magnetic Resonance
www.elsevier.com/locate/jmr

Three-dimensional cylindrical X-band ESR imaging by a combined pulsed gradient Fourier and static gradient projection reconstruction method

Michael Glied, Malte Drescher *, Elmar Dormann

Physikalisches Institut, Universität Karlsruhe (TH), D-76128 Karlsruhe, Germany

Received 8 November 2005; revised 13 January 2006
Available online 21 February 2006

Abstract

Static gradient electron spin echo projection reconstruction imaging is favourable for X-band material science applications requiring temperature variation with a metal cryostat. To prevent imaging artefacts due to the high conduction electron diffusion coefficient in the preferred conduction direction of quasi-one-dimensional conductors, only pulsed gradient phase encoding for that direction can be tolerated. We present results of an appropriate cylindrical imaging scheme combining both methods. Conduction electron spin density images with $13 \times 13 \times 17\ \mu m^3$ volume element size or spin–lattice relaxation time images with inversion recovery sequence and $13 \times 13 \times 68\ \mu m^3$ volume element size are presented for fluoranthene radical cation salt single crystals of typical sizes of $0.4 \times 0.4 \times 1\ mm^3$.

Keywords: ESR imaging; Projection reconstruction; Fourier imaging; Relaxation time imaging; Quasi-one-dimensional organic conductors

1. Introduction

One-dimensional organic metals like fluoranthene (FA) radical cation salts (e.g., $(FA)_2PF_6$) can be grown by electrochemical techniques [1] and analysed by pulsed ESR techniques [2]. However, their single crystals tend to exhibit growth sectors [3], or even holes in the center [4], and defects—statistically distributed or arbitrarily introduced by irradiation—can modify their physical properties drastically and spatially non-uniformly [4–6]. Thus an easy to apply ESR imaging technique, copying the advantages of NMR microscopy [7], is of particular interest. Three-dimensional pulsed ESR Fourier imaging has been applied to $(FA)_2PF_6$ in the radio frequency range using the fringe field of a superconducting magnet [8]. However, to improve signal to noise ratio by increased measuring frequency, the use of an electromagnet is required, furthermore metal cryostats are essential for temperature variation. Both allowing for eddy currents it turned out to be advantageous to abstain from pulsed gradients. Hence, spin echo detection in rotated static magnetic field gradients and the filtered back projection technique was easier to handle in two-dimensional pulsed ESR imaging [9]. Unfortunately, the "simple" extension to the three-dimensional version of filtered back projection imaging with static magnetic field gradient [10] is prohibited in quasi-one-dimensional conductors, because the conduction electron spin motion in the preferred direction (with 10^4:1 anisotropy of the diffusion coefficient) tends to give rise to imaging artefacts [11].

Therefore we tested and describe below a 3d pulsed X-band ESR imaging version that adopts a static magnetic field gradient rotated only in the plane perpendicular to the highly conducting direction of the organic conductor, and a pulsed gradient for phase encoding in the third direction [12]. Our report is organized as follows: in Section 2 we describe the principles of 3d cylindrical conduction electron spin imaging, the technical realization adopted here and the characteristics of the samples used for the test

* Corresponding author.
E-mail address: malte.drescher@pi.uka.de (M. Drescher).

1090-7807/$ - see front matter © 2006 Elsevier Inc. All rights reserved.
doi:10.1016/j.jmr.2006.02.005

experiments. In Section 3, we discuss the results on 3d spin density distribution and variation of the spin–lattice relaxation time achieved here for $(FA)_2PF_6$ single crystals. Our general results are emphasized in Section 4.

2. Experimental details

2.1. Principle of cylindrical imaging

For an introduction to magnetic resonance imaging we refer to standard textbooks [7,10]. The speciality of our approach is the cylindrical imaging frame. The principles of scanning $\vec{k}$ space [13]

$$\vec{k} = \frac{1}{2\pi}\gamma\vec{G}t \tag{1}$$

(with γ is the gyromagnetic ratio, $\vec{G}$ is the applied magnetic field gradient, and time t) in cylindrical coordinates can be explained based on Fig. 1. The method is a combination of 2d projection reconstruction and 2d Fourier imaging [7]. It uses a static x–z reading gradient rotated in the x–z plane and a pulsed y-gradient, in the direction of the rotation axis, defining a plane in $\vec{k}$ space. The static homogeneous magnetic field $\vec{B}_0$ is applied along the z axis. The signal $S(\vec{r}) = S(\rho, \phi, y)$ is obtained as

$$S(\vec{r}) = \int_0^{\pi}\int_{-\infty}^{+\infty}\int_{-\infty}^{+\infty} S(k_\rho, k_y, \phi) \times \exp[-i2\pi(k_\rho\rho + k_y y)]k_\rho\,dk_\rho\,dk_y\,d\phi \tag{2}$$

with $|k_\rho| = \sqrt{k_x^2 + k_z^2}$ and $\rho = z\cos\phi + x\sin\phi$.

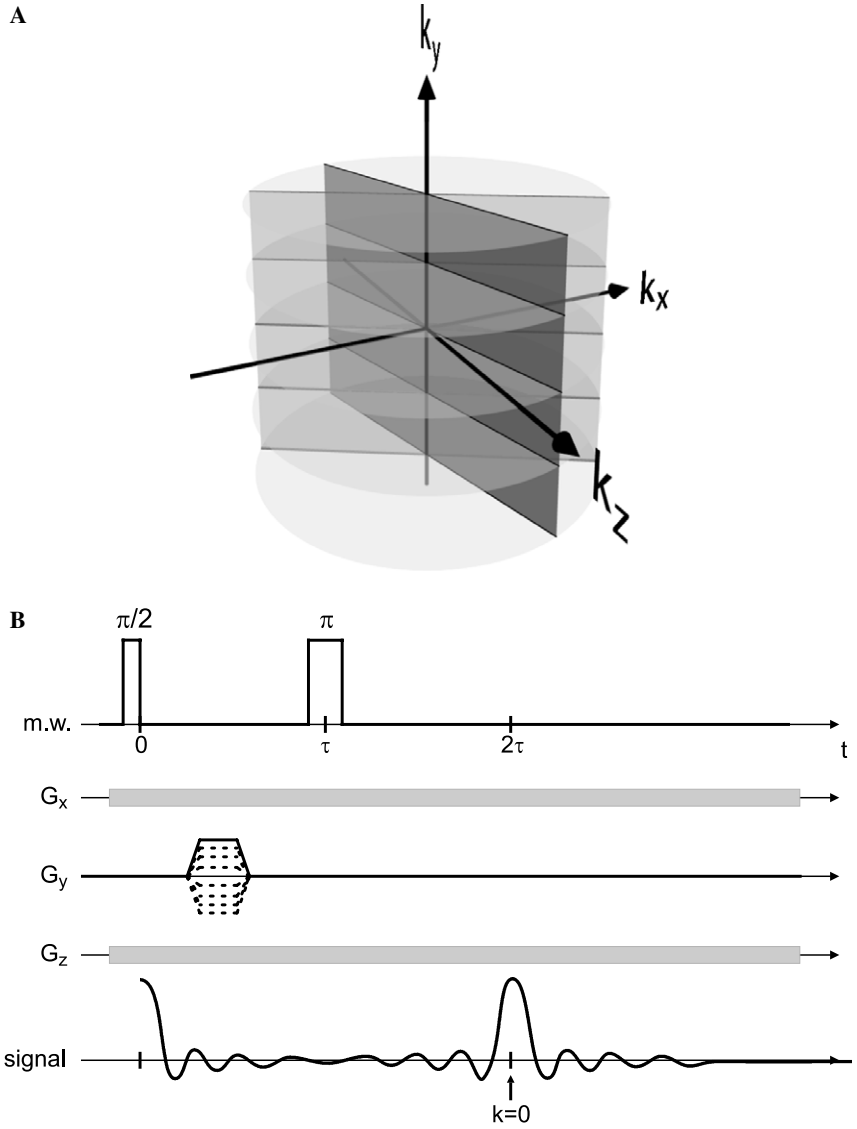

Fig. 1. Probing $\vec{k}$ space in cylindrical imaging. (A) Static gradients G_x and G_z define the orientation of planes scanned with pulsed G_y gradients, used for 2d Fourier imaging. These planes are rotated around the y-direction, allowing 3d imaging by filtered projection reconstruction. (B) Pulse scheme for cylindrical imaging: $\pi/2-\tau-\pi$ microwave pulse sequence, static gradient in x–z plane, by strength and duration of the G_y pulsed gradient the k_y-plane is encoded. Echo signal detection, with echo center defining $k = 0$.

We neglect for simplicity of the presentation, that relaxation and diffusion in presence of magnetic field gradients actually result in [14]

$$S(\vec{r},2\tau) = S(\vec{r},0)\cdot\exp\left(-\frac{2\tau}{T_2}-\frac{2}{3}D\gamma^2G^2\tau^3\right). \quad (3)$$

We showed before that spatially varying transversal relaxation rates T_2^{-1} or spin diffusion coefficients D can be determined reasonably accurately by analysing the τ dependent signal $S(\vec{r}_i,2\tau)$ of the individual volume element or pixel $\vec{r}_i$ [11,6]. The inner integral of Eq. (2) can be understood as a filtered profile $P^*_\phi(\rho,y)$, like in projection reconstruction. It presents a 2d Fourier transform of the k_ρ multiplied signal in planes of fixed angle ϕ. In our case of discrete scanning of the $\vec{k}$ space, only well defined y values are reconstructed and thus we obtain

$$S(x,y,z) = \Delta\phi\sum_{\phi_i} P^*_{\phi_i}(\rho(x,z,\phi_i),y). \quad (4)$$

The resolution in y-direction is determined by the strength and duration of the pulsed gradient G_y (Fig. 1B), with the field of view

$$y^{\max} = \frac{1}{\Delta k_y} \quad (5)$$

inversely proportional to the pulsed gradient step width and the resolution in y-direction of

$$\Delta y_i = \frac{1}{(N_y-1)\Delta k_y} \quad (6)$$

additionally related to the number N_y of y gradient steps used in the experiment.

For the x–z plane accessed by projection reconstruction, the Crowther theorem [15] may be used to estimate the accessible resolution, i.e.,

$$\Delta_{xz} = \frac{\pi d}{N_\phi}. \quad (7)$$

Here d is the diameter of the object to be imaged—below 0.5 mm for our $(FA)_2PF_6$ crystals—Δ_{xz} the resolution, and N_ϕ the number of one-dimensional projections. For 180 projections we estimate a resolution of $\Delta_{xz}\approx 10$ μm. We present data on a cartesian grid and interpolate only in the last step in real space. Therefore, in the x–z plane we could adopt unphysically small size of the volume elements and need the Crowther theorem as a rule. The field of view, on the other hand, is well defined by

$$\rho^{\max} = \frac{1}{\sqrt{2}\Delta k_\rho} = \frac{\sqrt{2}\pi}{\gamma(G_x^2+G_z^2)^{1/2}t_d} \quad (8)$$

with the dwell time t_d and the strength of the gradient as alternative control parameters. Anisotropy of the g tensor and conduction electron diffusion may reduce the achievable resolution. To minimize the latter influence, short τ values (Fig. 1B) are preferred, requiring short G_y gradient pulses.

This imaging scheme can be combined with the familiar pulsed magnetic resonance methods delivering—now spatially resolved—T_1 or T_2 relaxation times. As an example, we show below spatially resolved spin–lattice relaxation times, $T_1(\vec{r}_i)$, obtained by use of the inversion recovery sequence, with a π pulse preceding, by varied recovery or readout times T, the sequence shown in Fig. 1B (10 different values).

2.2. Experimental realization

The pulsed ESR imaging results were obtained with a Bruker Elexsys E580 spectrometer at about 9.6 GHz, using an ER4118X-MD5 dielectric ring resonator with 5 mm inner diameter of the sample space, installed inside an ER4118CF continuous flow cryostat, using for the examples shown below liquid nitrogen as cooling agent. The pulse length of the π/2 pulse amounted to 12 ns. 1024 data points were typically recorded for each gradient setting with $\tau = 3$ μs, with a dwell time $t_d = 10$ ns, using a 16-fold phase cycling, and accumulating up to 1000 scans. Hall regulation of the magnetic field strength of the electromagnet, cooled via heat exchanger, gave sufficient long time stability in spite of the extremely narrow ESR line width of only about 1.5 μT [2] of the samples studied. A static gradient of $G_\rho = G_z = 0.56$ T/m along the main field direction was produced with two soft iron wedges on one of the pole caps of the electromagnet. Instead of rotating the static gradient around the y axis in the x–z plane (Fig. 1), the sample was rotated around the y axis with help of a goniometer for spatially fixed, static G_ρ. The ER218G1 goniometer allows an accuracy of $\delta\phi = 1/4°$. Thus only $\Delta\phi = 4°$ steps were used below. The pulsed gradient G_y was realized with a pair of "8" shaped 0.1 mm thick copper loops of about 7 mm total extension (each with double turns and connected via twisted leeds), fixed with two component epoxy resin between two 50 μm thick plastic films. After being bent into cylindrical form they were introduced into the inner 5 mm bore of the cavity more than 5 mm apart from the metallic walls of the cavity. The measured total inductance of coils and leads amounts to $L = 1.1$ μH.

For one current polarity, e.g., $+I_0$, this arrangement increases the B_z strength for positive y values and reduces it for negative y values. The static calibration indicated sufficient linearity of $B_z(y)$ with $G_y = \frac{\partial B_z}{\partial y} = 0.23\cdot I_0$ (where the gradient is in T/m and I_0 is in A), useful for -1.4 mm $< y < +1.4$ mm. This arrangement is capable of quasi static currents (200 μs) of 1.6 A and pulsed gradients of 1 T/m and about 1.5 μs length without breakdown. As usual, the gradient pulses were produced with a pulse driver based on the "clipped L-C resonant circuit" idea [16,8,9]. Maximum phase encoding values of

$$k_y = \frac{1}{2\pi}\gamma\int_0^{t_p} G_y(t)\,dt \quad (9)$$

of $k_y = N_y \cdot \Delta k_y = 29\ \mathrm{mm}^{-1}$ were realized for 75 V charging of the capacitors, with $N_y = 64$ steps set manually. In y-direction, a field of view of 1.1 mm and a resolution of 17 μm is thus realized according to Eqs. (5) and (6). In spite of the distance of gradient coils to the metallic surrounding the decay of eddy currents must be awaited. Thus the pulse separation time $\tau = 500$ ns commonly used for this buildup has to be increased to $\tau = 3$ μs and therewith a loss of about 50% signal intensity has to be taken. A home-build software package for 2d image reconstruction written in C was adapted for the algorithm of cylindrical imaging introduced in Section 2.1 [9,12]. To correct for a possible out of rotation axis mounting of the sample, the centers of gravity of the one-dimensionally projected signals $S(\rho,\phi)$ and $S(\rho,\phi+\pi)$ were centered numerically. Rendering of the data was realized by commercial visualization software.

2.3. Sample characterization

The imaging scheme was tested with samples of the radical cation salts of fluoranthene (i.e., $(FA)_2PF_6$), perylene (i.e., $(PE)_2AsF_6 \cdot 2/3$ tetrahydrofurane) and naphthalene (i.e., $(NA)_2PF_6$). For clarity, we restrict this report to two examples of $(FA)_2PF_6$ single crystal imaging. We mention, however, that T_2 imaging, or analysis of sample aging by extended exposure of crystals to air at room temperature were successfully performed as well [12]. The geometrical parameters of the two $(FA)_2PF_6$ crystals were A: $0.5 \times 0.5 \times 0.7\ \mathrm{mm}^3$, B: $0.2 \times 0.2 \times 1.25\ \mathrm{mm}^3$, with the largest dimension parallel to the highly conducting FA stacking direction. These $(FA)_2PF_6$ crystals were grown by electrocrystallization along the established procedures [1,17]. We selected hollow crystals with shiny black surfaces, preventing thus problems related with the skin depth (microwave conductivity $\sigma_\parallel \approx 50\ \mathrm{S\,cm}^{-1}$, anisotropy $\sigma_\parallel$: $\sigma_\perp > 100{:}1$). Due to varying defect concentration in the range of about 1 Curie-like defect per 1000 formula units, the conduction electron spin relaxation times T_1 and T_2 (of about 8 μs) and the diffusion coefficient ($D_\parallel \approx 1\ \mathrm{cm}^2/\mathrm{s}$) are spatially non-homogeneous in these samples [4], whereas orientation of the crystal axes is uniform [3]. Thus they present valuable model systems for imaging attempts. $(FA)_2PF_6$ crystals have a Peierls-like metal–non-metal transition at $T_p = 186$ K [3,18]. The conduction electron spin resonance measurements presented below were therefore performed at $T = 250\ \mathrm{K} > T_p$, close to the crystal growth temperature, and thus sufficiently below room temperature for improved sample stability.

3. Discussion of the results

For demonstration of the performance of the cylindrical imaging scheme, we selected and present two examples: on the one hand the derivation of a three-dimensional conduction electron spin density image is demonstrated for sample A in Section 3.1, on the other hand the distribution of the conduction electron spin–lattice relaxation time T_1 in another single crystal of the organic conductor $(FA)_2PF_6$ (sample B) is shown in Section 3.2. For clarity of the discussion and facilitation of the examination of the experimental conditions, we compile all relevant parameters in Table 1.

Table 1
Parameters used for 3d cylindrical imaging examples discussed in Section 3

Sample	A ($S(z,x,y)$)	B ($T_1(z,x,y)$)
Volume element		
$z \times x \times y/\mu\mathrm{m}^3$	$12.9 \times 12.9 \times 17.2$	$12.7 \times 12.7 \times 67.7$
Field of view		
ρ/mm	4.48	2.50
Zoomed	1.28 (Zoom 3.5×)	0.62 (Zoom 4×)
y/mm	1.09	2.10
$\pi/2$; π pulse lengths (ns)	16; 32	12; 24
τ (μs)	3	3
Repetition time (μs)	500	500
Inversion recovery T values (μs)	—	0.1, 3.1, . . ., 27.1
Dwell time t_p (ns)	10	20
Length of data set	1024	512
Phase cycles	16	16
Scans per gradient settings	500	100
G_ρ (T/m)	0.563	0.505
N_ϕ; $\Delta\phi$	45; 4°	18; 10°
G_y/I_0 (T/m A)	0.226	0.257
$G_y^{\max}$ (T/m)	1.012	0.494
$k_y^{\max}$ (mm^{-1})	29.47	7.60
N_y	64	32

3.1. Spin density imaging

Fig. 2A shows an optical image of the $(FA)_2PF_6$ single crystal "sample A." It shows the typical outer habitus of the surfaces that are oriented parallel to the FA stacking direction a (long side) [3–5], but this is a hollow crystal with tubular cavity parallel to a, open at both ends. For the presentation of the 3d-ESR imaging spin density distribution results, only 2d paper surfaces are available here. Thus there is the choice between the visualization of various 2d sections, as is used for the T_1-images below, or the perspective presentation of all volume elements with intensities above a preset level, with varied viewing angle. The latter version is used for Figs. 2B and C and the accompanying on-line video clip, allowing to vary the viewing angle. 25% up to the maximum signal strength was selected for the rendering of these images. We would like to mention that in this case spin density means actually transverse magnetization, because both are non-trivially related in a one-dimensional metal with Pauli-paramagnetism modified by charge density wave fluctuations announcing the Peierls transition towards a low-temperature non-metallic state. The image is additionally slightly T_2 weighted due to the use of a finite pulse separation time $\tau = 3$μs, although the T_2 of $(FA)_2PF_6$ is long ($T_2 \approx 8$ μs [2,19]).

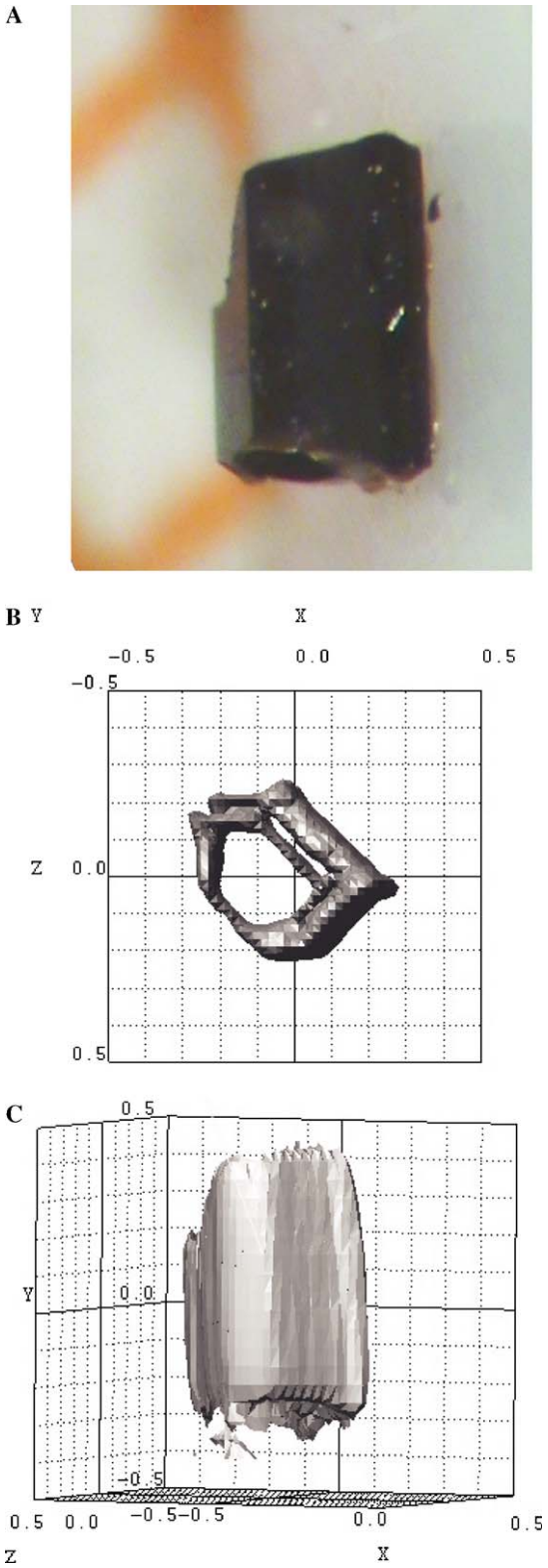

Fig. 2. $(FA)_2PF_6$ crystal, sample A. (A) Optical image, with crystallographic a axis vertical, with length $l \approx 0.7$ mm (B), (C) ESR spin density image showing all volume elements with 25–100% of maximum intensity, seen parallel (B) or perpendicular (C) to the y axis (corresponding to the highly conducting a axis of the crystal). In the on-line version, a video clip allows inspection of sample A under varied angles of view. For imaging parameters see Table 1.

Fig. 2 as well as the video prove the high reliability of the reproduction of angles and length scales by the 3d cylindrical imaging scheme, as well as the absence of major imaging artefacts.

3.2. Spin–lattice relaxation imaging

ESR imaging merits only the effort of its introduction to material science, if, or because, relevant microscopic physical parameters can be derived quantitatively and visualized for a graphic interpretation. In one-dimensional organic conductors, inevitable growth defects of small relative concentration of 10^{-5} to 10^{-3}. Curie paramagnetic defects per formula unit influence the conduction electrons nevertheless dramatically, because the anisotropy of their mobility of at least 10^4:1 prevents the conduction electron from escaping an obstacle encountered on its one-dimensional path. This is reflected in the defect dependence of T_2, T_1, and D for the conduction electrons in arene radical cation salts. Unfortunately, even variations of these quantities by a factor of 2 inside a macroscopic single crystal are difficult to unravel in integral measurements of the whole crystal. For the $(FA)_2PF_6$ single crystal, sample B, analysed here, the integral T_1 measurement at 250 K gave $T_1 = 6.85 \pm 0.15$ μs, with no really suspicious deviations of the data fit. On the other hand, Figs. 3 and 4 demonstrate easily the characteristic spatial variation of T_1, visualized by colour code on the right hand sided cross-sections 3A–D, in contrast to the independent variation of the signal strength in the left hand part of these figures. For all individual volume elements of sample B, reliable inversion recovery fits, as exemplified in Fig. 4 for the shortest and longest recovery, could be performed "automatically." Instead of applying phase correction the absolute value of the signal strength was used. The fitting routine derives unphysical T_1-data also for the volume elements that reflect only the noise level, however. Thus, for the right hand part of Fig. 3 only those volume elements (or pixels) are presented, whose spin density (left part) is above an adjustable level, set here to 25% of the maximum. The average of T_1^{-1} rates of all these volume elements of the 3d ESR image gave $T_1 = 6.71$ μs, in accordance with the integral value given above. Evidently, images like Figs. 2 and 3 are very useful for material characterization, because they prevent the application of oversimplified models to the description of the physical properties of these fascinating organic metals.

4. Conclusions

We introduced a new version of X-band pulsed ESR 3d imaging with a cylindrical imaging frame, that is extremely easy to realize. In its most spartanic version, exemplified above, a constant static gradient in main field direction and a pulsed gradient along a perpendicular sample rotation axis are sufficient for the implementation. The basic principle is the combination of 2d Fourier imaging and 2d filtered back projection reconstruction. Resolution and field of view

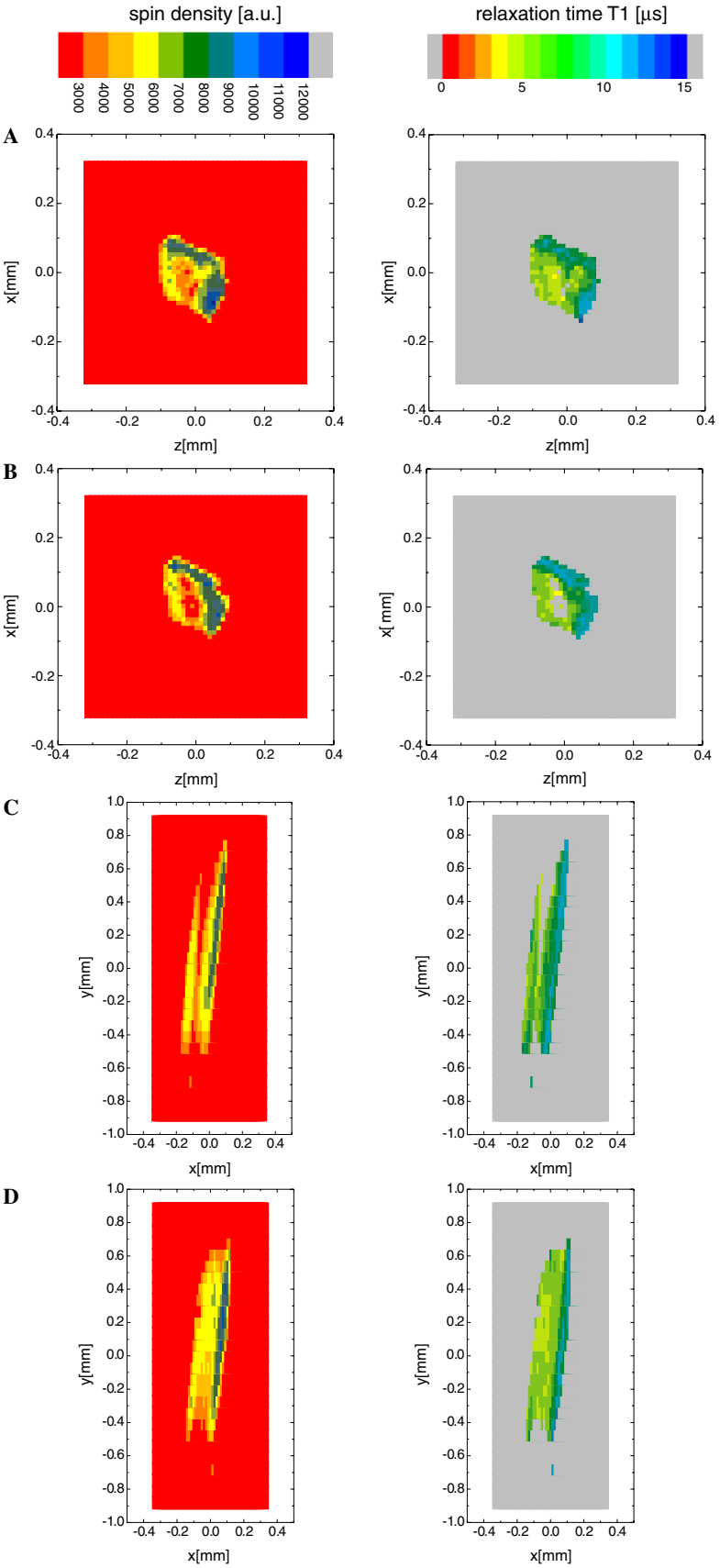

Fig. 3. Examples of sections across the 3d-ESR image of sample B, obtained by the cylindrical imaging scheme with the parameters given in Table 1. The coordinate system is introduced in Fig. 1A, the color code is defined on top of the figure. Left part gives spin density, right part the T_1-variation for the same cross-section. Two sections parallel to the z–x plane at $y = 0.000$ (A) and $y = +0.407$ mm (B), and two sections parallel to the x–y plane at $z = +0.0064$ mm (C) and $z = -0.0573$ mm (D) are given.

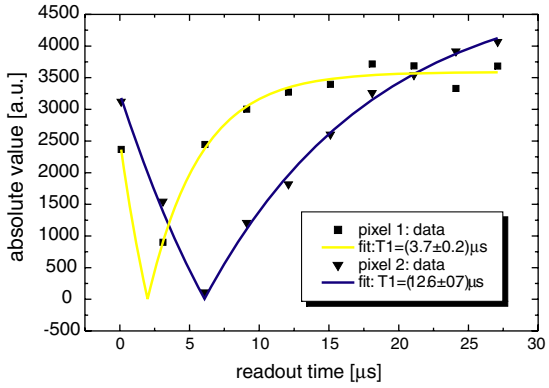

Fig. 4. Two examples of the raw data (absolute value of signal strength versus recovery or readout time T) and inversion recovery fit (coloured line) used to derive the spin–lattice relaxation time T_1 for an individual volume element, with the line fit visualized by the colour code used in Fig. 3. Both volume elements are taken from Fig. 3A: "pixel 1," with the shortest T_1 at ($x = -0.0064$ mm, $y = 0$, $z = -0.0319$ mm), and "pixel 2," with the longest T_1, at ($x = -0.1338$ mm, $y = 0$, $z = 0.0446$ mm).

in the plane and along the cylinder axis can independently and reliably be controlled. We showed the performance of this imaging scheme for non-ideal single crystals of a quasi-one-dimensional organic conductor, visualizing the imaging of T_2 weighted conduction electron spin density and of the inhomogeneous distribution of the spin–lattice relaxation time T_1 with measurements requiring a metal cryostat for temperature control. This imaging scheme is especially appropriate for materials with highly anisotropic spin mobility and could be fully automated by use of a computer controlled goniometer. Since only a minor number of "home made" additions to a standard commercial pulsed ESR spectrometer are required, this cylindrical 3d imaging frame might open access to spatially resolved resonance analysis in various other areas of research.

Acknowledgments

We thank N. Kaplan, M. Ulrich, and T. Wokrina for discussions, J. Gmeiner for crystal growth and the Deutsche Forschungsgemeinschaft for financial support (Grant Do 181/10-3).

Appendix A. Supplementary data

Supplementary data associated with this article can be found, in the on-line version, at doi:10.1016/j.jmr.2006.02.005.

References

[1] C.H. Kröhnke, G. Wegner, V. Enkelmann, Radikalkaltionensalze einfacher Arene - eine Familie organischer Metalle, Angew. Chem. 92 (1980) 941.
[2] G. Sachs, W. Stöcklein, B. Bail, E. Dormann, M. Schwoerer, Electron spin relaxation of new organic conductors: fluoranthenyl radical cation salts, Chem. Phys. Lett. 89 (1982) 179.
[3] C. Buschhaus, J. Gmeiner, H. Henke, M. Ulrich, E. Dormann, Structural origin of inhomogeneous properties in (fluoranthene)$_2$PF$_6$ crystals, Synth. Metals 149 (2005) 89.
[4] T. Tashma, A. Feintuch, A. Grayevsky, J. Gmeiner, A. Gabay, E. Dormann, N. Kaplan, Mapping the dynamic properties of electron spins in the organic conductor (FA)$_2$PF$_6$, Synth. Metals 132 (2003) 161.
[5] T. Wokrina, J. Gmeiner, N. Kaplan, E. Dormann, Sample Dependence of Anisotropy and Restriction of Electron-Spin Diffusion in the Quasi-One Dimensional Organic Conductor (Fluoranthene)$_2$PF$_6$, Eur. Phys. J. B 35 (2003) 191.
[6] M. Drescher, N. Kaplan, E. Dormann, Zebralike patterned organic conductor with periodic modulation of mobility and peierls transition, Phys. Rev. Lett. 94 (2005) 016404.
[7] P.T. Callaghan, Principles of Nuclear Magnetic Resonance Microscopy, Oxford University Press, Oxford/New York, 1991.
[8] A. Feintuch, G. Alexandrowicz, T. Tashma, Y. Boasson, A. Grayevsky, N. Kaplan, Three-dimensional pulsed ESR fourier imaging, J. Magn. Res. 142 (2000) 382.
[9] M. Ulrich, T. Wokrina, M. Drescher, E. Dormann, Comparison of 2d ESR imaging techniques in two frequeny ranges, Appl. Magn. Reson. 29 (2005) 385.
[10] P.G. Morris, Nuclear Magnetic Resonance Imaging in Medicine and Biology, Clarendon Press, Oxford, 1986, p. 135 ff.
[11] T. Wokrina, E. Dormann, 2d ESR diffusion coefficient imaging with the projection reconstruction method, J. Magn. Reson. 167 (2004) 114.
[12] M. Glied, Diplomarbeit, Dreidimensionale Bildgebung mit gepulster Elektronenspinresonanz, Universität Karlsruhe (TH) (2005).
[13] P. Mansfield, P.K. Grannel, NMR 'diffraction' in solids? J. Phys. C 6 (1973) L422.
[14] H.Y. Carr, E.M. Purcell, Effects of diffusion on free precession in NMR experiments, Phys. Rev. 94 (1954) 630.
[15] R.A. Crowther, D.J.D. Rosier, A. Klug, The reconstruction of a three-dimensional structure from projections and its application to electron microscopy, Proc. Roy. Soc. London A 317 (1970) 319.
[16] M. Conradi, A.N. Garroway, D.G. Cory, J. Miller, Generation of short, intense gradient pulses, J. Magn. Reson. 94 (1991) 370.
[17] V. Enkelmann, Radical-cation salts of arenes. A new family of organic metals, Adv. Chem. Ser. 217 (1988) 177.
[18] U. Köbler, J. Gmeiner, E. Dormann, High Field Magnetic Susceptibility of Individual Single Crystals of the Organic Conductor (Fluoranthene)$_2$PF$_6$, J. Magn. Magn. Mater. 69 (1987) 189.
[19] E. Dormann, G. Denninger, G. Sachs, W. Stöcklein, M. Schwoerer, Application of the organic conductor (fluoranthene)$_2$PF$_6$ as an ESR magnetic field probe, J. Magn. Magn. Mater. 54–57 (1986) 1315.